Composite Structures 201 (2018) 261–275

Contents lists available at ScienceDirect

Composite Structures

journal homepage: www.elsevier.com/locate/compstruct

3D explicit finite element analysis of tensile failure behavior in adhesive-bonded composite single-lap joints

Jinxin Ye[a,b,*], Ying Yan[a], Jie Li[a], Yang Hong[a], Ziyang Tian[a,b]

[a] School of Aeronautic Science and Engineering, Beihang University, Beijing 100191, China
[b] Shenyuan Honors College, Beihang University, Beijing 100191, China

ARTICLE INFO

Keywords:
Adhesive-bonded joints
Explicit analysis
Finite element methods (FEMs)
Failure modes

ABSTRACT

The tensile failure behavior in adhesive-bonded composite single-lap joints with different overlap lengths is investigated through experiments and various three-dimensional (3D) explicit finite element methods (FEMs). Different failure modes are observed in different overlap lengths. Three parameterized finite element models are developed to discuss the accuracy and applicability of the 3D explicit FEMs based on different modeling strategies and improved failure criteria. All criteria are programmed with the explicit user subroutines employing element deletion to avoid convergence problems caused by element distortion. The load-displacement curves predicted by these models are consistent with the experimental results, while the prediction of failure morphology depends on model types. The models neglecting interface elements cannot simulate the delamination when cohesive zone models (CZMs) are adopted to predict adhesive failure. The influence of CZMs on delamination is analyzed comprehensively to address this problem. Analysis of stress distribution in an overlap of a length of 10 mm indicates that the peak stress of the adhesive layer occurs on the overlap ends along the axial direction, coinciding with implicit results.

1. Introduction

Compared with the traditional mechanical joints, adhesive-bonded joints have the advantages such as lighter weight and smoother aerodynamic shape. Thus, the adhesive-bonded composite single-lap joint, as one of the low-cost and simple fundamental adhesive-bonded joints, has been widely used in the design of advanced composite structures.

Since the 1930s, research on adhesive-bonded composite joints has attracted increasing attention, and some theoretical investigations have been conducted [1–6]. Subsequently, many studies [7–13,19–21] have been carried out by FEMs to predict the failure load, stress distribution and damage propagation of adhesive-bonded joints. Harris et al. [7] proposed a non-linear finite element technique based on the plane strain assumption to predict the failure load of single-lap joints. Pickett et al. [8] used two analytical methods to determine distribution of elastic-plastic adhesive stress in bonded joints. The effect of various parameters on the performance of adhesive-bonded joints is studied in Ref. [9] by Gunnion and Herszberg. They found that an added overlaminate could reduce the peak stress in the adhesive. To simulate failure behaviors better, special elements and failure criteria were also developed by several scholars. Andruet et al. [10] developed special adhesive elements for load-displacement analyses, and represented the adherend with shell elements. Gonçalves et al. [11] established a new model for finite element analysis of single-lap joints using developed interface elements. Wahab et al. [12] proposed a damage criterion based on thermodynamics principles, and Anyfantis et al. [13] proposed a new T-S criterion to simulate the mixed-mode failure of the ductile adhesive layer. In recent years, CZMs have been used to model thin adhesive layers or adherend-adhesive interfaces in bonded joints. Blackman et al. [14] applied CZMs to bonded composite configurations and investigated the physical significance of the maximum stress. Li et al. [15,16] used CZMs to model the mixed-mode fracture of adhesive-bonded joints. In their subsequent works, they showed that the CZMs can predict both strength and failure mechanism of joints. Moura et al. [17] used cohesive and continuum mixed-mode damage models to simulate damage propagation of bonded joints. Li et al. [18] and Luo et al. [19] performed finite element analyses to investigate the tensile failure behavior of adhesive-bonded joints with implicit methods. They used the same method to simulate the delamination with cohesive elements, and the laminates with shell elements.

Most scholars use implicit methods to analyze bonded joints. Severe convergence problems caused by divergent results of iterative computations and ill-conditioned solutions for simultaneous equations might easily occur in implicit FEMs, resulting from complicated distribution of

* Corresponding author at: School of Aeronautic Science and Engineering, Beihang University, Beijing 100191, China.
E-mail address: yejinxin521@126.com (J. Ye).

https://doi.org/10.1016/j.compstruct.2018.05.134
Received 24 August 2017; Received in revised form 19 May 2018; Accepted 28 May 2018
Available online 15 June 2018

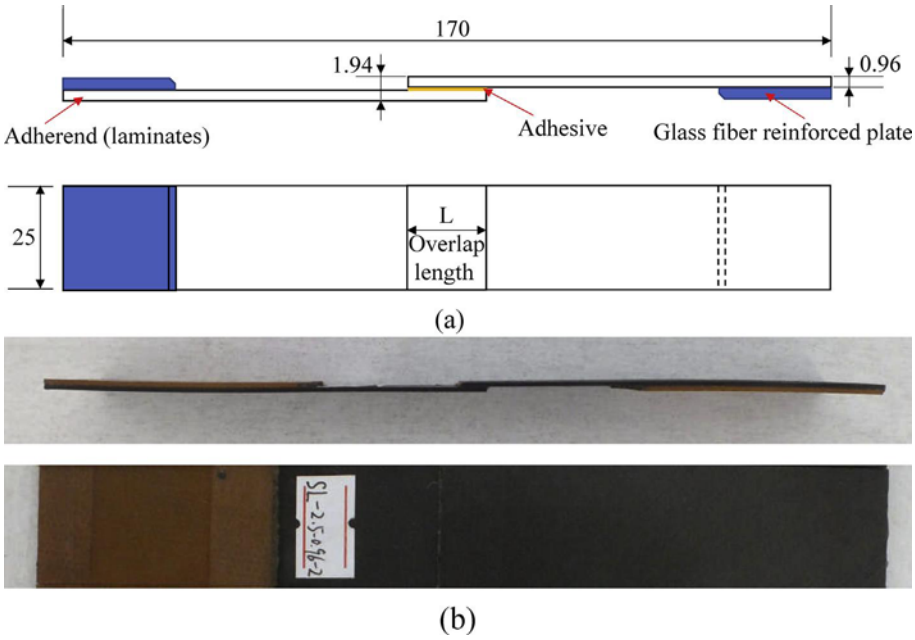

Fig. 1. Geometry of test specimens (unit: mm): (a) Diagram of specimens; (b) Photograph of specimens.

Table 1
Information of the specimens.

Group	Overall size (mm)	Adherend thickness (mm)	Overlap length L(mm)	Number of the specimens	Adherend stacking sequences	
					Upper	Lower
A	170 × 25	0.96	2.5	6	$[45/0/-45/90]_S$	$[-45/0/45/90]_S$
B	170 × 25	0.96	5.0	6		
C	170 × 25	0.96	10.0	6		

Table 2
Properties of T300/QY8911.

Elastic property	Value	Strength property	Value
E_{11} (GPa)	135	X_T (MPa)	1548
E_{22} (GPa)	8.8	X_C (MPa)	1226
E_{33} (GPa)	8.8	Y_T (MPa)	55.5
G_{12} (GPa)	4.47	Y_C (MPa)	218
G_{13} (GPa)	4.47	S_{12} (MPa)	89.9
G_{23} (GPa)	4.00	S_{13} (MPa)	89.9
ν_{12}	0.33	S_{23} (MPa)	51.2
ν_{13}	0.33	Density ρ (kg/m^3)	1600
ν_{23}	0.35		

Table 3
Properties of J116B.

Property	Shear strength (MPa)	Peel strength (90°) (kN/m)	Density ρ (kg/m^3)
Value	24.5	7.5	1000

stress and failure modes around adhesive regions. The convergence problems can be solved better by explicit FEMs, which can be used to perform quasi-static analysis [20]. A few studies have been conducted by using explicit solvers to model adhesive-bonded joints. For example, Neumayer et al. [21] presented an explicit cohesive element to enable the simulation of delamination in bonded joints on a full-scale structural level. However, these explicit methods are relatively incomprehensive and are mostly based on 2D elements. The efficiency and reliability of different types of explicit FEMs remained unknown in terms of damage of 3D elements, and possible convergence problems caused by 3D element distortions [22] were generally not considered in these methods either. Thus, further studies are needed to be investigated.

The objective of this paper is to present a comprehensive study of the tensile failure behavior in adhesive-bonded composite single-lap -joints. Single-lap joints with different overlap lengths are tested under a uniaxial tension load, and three types of parameterized 3D explicit models are established with user subroutines. Element deletion is adopted in user subroutines to overcome the convergence problems caused by element distortion. By comparing numerical results with experimental data, efficiency and accuracy of these models are comprehensively discussed in terms of load-displacement curves and failure morphology. The applicability of different explicit FEMs is also discussed based on different failure modes. Besides, the effect of cohesive elements on delamination is analyzed, and stress distribution of explicit models is compared with the implicit results.

2. Experiment

2.1. Specimens and experimental test methods

Specimens were made up of adherends and adhesive, and adherends were constituted by fiber-reinforced composite laminates consisting of fibers and polymer matrix. Fig. 1 and Table 1 display the geometry of the specimens. These specimens were divided into three groups, with each group containing six pieces. The overall sizes of all specimens were the same, with the length being 170 mm, the width being 25 mm, and the average thickness being 1.94 mm. But each group has different overlap length L (Group A: L = 2.5 mm, Group B: L = 5.0 mm, and Group C: L = 10.0 mm). The adherend consisted of eight layers, and the average thickness of the adhesive layer was 0.02 mm. The material of the adherend is T300/QY8911 (carbon fiber/BMI) with quasi-isotropic lay-ups ($[45/0/-45/90]_S$ or $[-45/0/45/90]_S$), and the material of the adhesive is J116B. The properties of the materials are presented in Tables 2 and 3. Besides, glass fiber-reinforced plates were appended on both ends of the joints to avoid damage of the clamping ends during loading.

The same axial tensile test of each specimen was performed to obtain reliable experimental results. The referenced test criteria are the

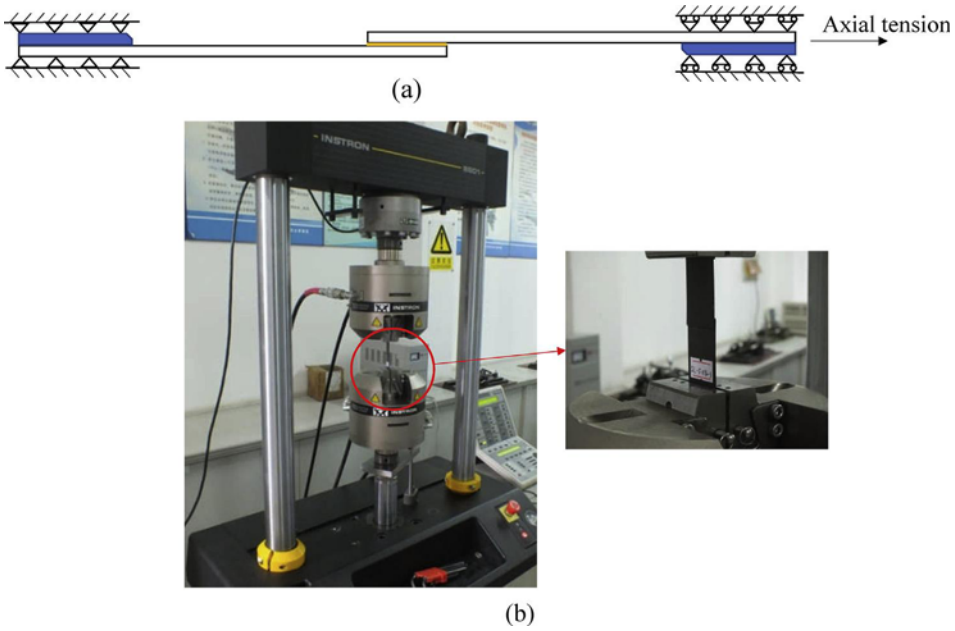

Fig. 2. Test set-up of specimens: (a) Diagram of specimens under the axial tension load; (b) Test system.

standard test methods ASTM D3039/3039 M, applying to polymer matrix composites. All tests were performed under quasi-static axial tension on an Instron 8801 hydraulic testing machine at room temperature 25 °C and were conducted in displacement loading control at a rate of 0.5 mm/min. The set-up for the tensile test is shown in Fig. 2.

2.2. Experimental results

Fig. 3 shows the failure morphology of adhesive-bonded composite single-lap joints. It can be observed that the failure modes of the three groups are different, and can be divided into three types: Mode A (adhesive failure), Mode B (mixed failure) and Mode C (delamination, fiber pull-out and fiber fracture). Mode B is a mixture of Mode A and Mode C. The statistical results of failure modes of each group are shown in Table 4.

The mainly failure morphology of Group A is Mode A (Fig. 3(a)), and the damage in the adhesive region (Region A-1 and Region A-2) is smooth, accompanied by no obvious damage of the adherend. But for Group C (Fig. 3(c)), it can be seen that the composite layer adjacent to the adhesive is peeled off, but the adhesive remains intact and reliable. Delamination extends between the first two layers of the lower plate (Region C-1 and Region C-2). Meanwhile, a small scale of delamination can be observed in the upper plate (Region C-3). A lot of fibers are pulled out along the fiber direction of the superficial composite layer, and some fibers are torn and broken at the edge of the overlap area (Region C-3 and Region C-4). For Group B (Fig. 3(b)), the failure Mode B is observed, which is a combination of adhesive failure and delamination. The damage is divided into two sections along the overlap area (e. g. Region B-1 and Region B-3), and some fibers are also pulled out. Besides, the failure load as well as displacement of the longitudinal failure gradually increase from Group A to Group C as the overlap length increases from 2.5 mm to 10.0 mm.

3. Explicit analysis

3.1. Failure criteria and damage evolution laws

Three types of 3D explicit finite element models (Model I, Model II and Model III) are established by different modeling strategies and failure criteria in this study. A detailed comparison of failure criteria in the three models is shown in Table 5.

In Model I, laminates follow improved 3D Hashin failure criteria with an exponential progressive damage evolution law proposed by Linde et al. [23]. As is known, the general 3D Hashin failure criteria [24,25] are stress-based. Some problems may occur when the stress-based failure criteria are applied to numerical calculations: the internal stress of the material tends to mutate along with the composite damage, and the stress mutation may lead to instability of numerical calculations especially with interface elements [26]. To overcome the problem, this paper refers to the research of Wang et al. [27] and expresses the improved 3D Hashin failure criteria with strains. Besides, this paper develops the general 3D Hashin failure criteria by introducing a first-order item of $\varepsilon_2 + \varepsilon_3$ in the matrix tensile failure formula, which can avoid a discontinuity of the failure enveloping surface under the condition of complex stress and predict the failure modes more accurately. The improved failure criteria are listed in Table 6. F_{ft}, F_{fc}, F_{mt} and F_{mc} are the damage initiation coefficients of different failure types. The initial damage of materials occurs when the corresponding coefficients equal 1. ε_{1t}^f, ε_{1c}^f, ε_{2t}^f, ε_{2c}^f and $\gamma_{ij}^f (i, j = 1, 2, 3)$ are failure strains, and can be calculated from failure strengths respectively as follows:

$$\varepsilon_{1t}^f = X_t/C_{11}, \quad \varepsilon_{1c}^f = X_c/C_{11}, \quad \varepsilon_{2t}^f = Y_t/C_{22}, \quad \varepsilon_{2c}^f = Y_c/C_{22}, \quad \gamma_{ij}^f = S_{ij}/G_{ij} \quad (i, j = 1, 2, 3) \tag{1}$$

where X_t, X_c, Y_t, Y_t and $S_{ij} (i, j = 1, 2, 3)$ are the corresponding failure strengths. Once the above criterion is satisfied, the corresponding exponential progressive damage evolution law evolves by calculating the damage variable as follows:

Fiber tension failure $\varepsilon_1 > 0$:

$$d_{ft} = 1-(1/F_{ft})\exp(-X_t\varepsilon_{1t}^f L^c(F_{ft}-1)/G_{ft}) \tag{2}$$

Fiber compression failure$\varepsilon_1 > 0$:

$$d_{fc} = 1-(1/F_{fc})\exp(-X_c\varepsilon_{1c}^f L^c(F_{fc}-1)/G_{fc}) \tag{3}$$

Matrix tension cracking $\varepsilon_2 + \varepsilon_3 > 0$:

$$d_{mt} = 1-(1/F_{mt})\exp(-Y_t\varepsilon_{2t}^f L^c(F_{mt}-1)/G_{mt}) \tag{4}$$

Matrix compression cracking $\varepsilon_2 + \varepsilon_3 < 0$:

$$d_{mc} = 1-(1/F_{mc})\exp(-Y_c\varepsilon_{2c}^f L^c(F_{mc}-1)/G_{mc}) \tag{5}$$

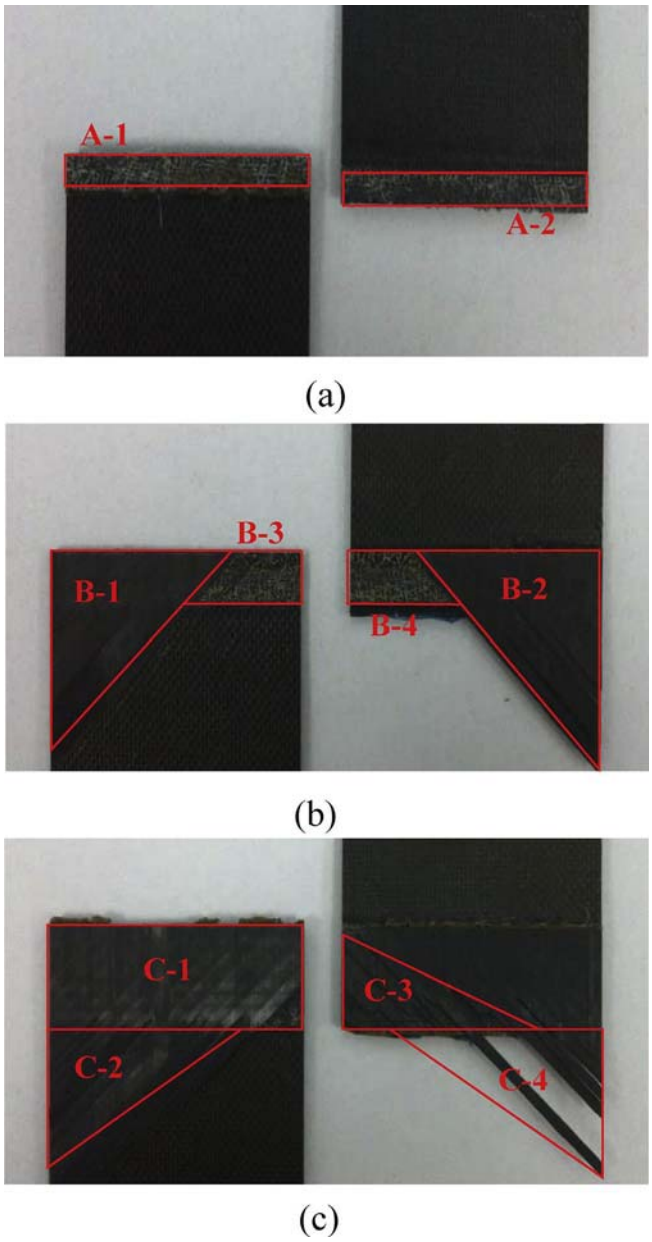

Fig. 3. Failure morphology of adhesive-bonded composite single-lap joints with different overlap lengths: (a) Mode A (L = 2.5 mm); (b) Mode B (L = 5.0 mm); (c) Mode C (L = 10.0 mm).

Table 4
Detailed failure modes with different test parameters.

Group	Overlap length L(mm)	Number of the specimens	Failure mode	Morphology	Average failure load (kN)	Average longitudinal failure displacement (mm)
A	2.5	6	Mode A	Fig. 3(a)	1.85	0.25
B	5.0	6	Mode B	Fig. 3(b)	3.61	0.45
C	10.0	6	Mode C	Fig. 3(c)	6.08	0.75

where d_{ft}, d_{fc}, d_{mt} and d_{mc} are the damage variables of different failure types; G_{ft}, G_{fc}, G_{mt} and G_{mc} are the corresponding fracture energy; L_c is the characteristic length associated with the material point. The fracture energy and the characteristic length can effectively overcome the mesh-dependence problems in FEMs [28]. Once the material is damaged, its stiffness matrix is weakened by the damage variables, and the constitutive relationship is updated as [29]

$$\boldsymbol{\sigma} = \begin{pmatrix} (1-d_f)C_{11} & (1-d_f)(1-d_m)C_{12} & (1-d_f)C_{13} & & & \\ & (1-d_m)C_{22} & (1-d_m)C_{23} & & 0 & \\ & & C_{33} & & & \\ & & & (1-d_f)(1-d_m)C_{44} & & \\ & sym & & & C_{55} & \\ & & & & & C_{66} \end{pmatrix} \boldsymbol{\varepsilon} \tag{6}$$

Where $C_{ij}(i, j = 1, 2, 3)$ are the stiffness coefficients of the undamaged material; d_f and d_m are the synthetical damage variables of fibers and matrix respectively, and are defined as

$$d_f = \begin{cases} d_{ft}, & \varepsilon_1 > 0 \\ d_{fc}, & \varepsilon_1 < 0 \end{cases}; \quad d_m = \begin{cases} d_{mt}, & \varepsilon_2 + \varepsilon_3 > 0 \\ d_{mc}, & \varepsilon_2 + \varepsilon_3 < 0 \end{cases} \tag{7}$$

All the above mentioned criteria are implemented in a user subroutine VUMAT [30].

Obviously, delamination is not considered in the 3D Hashin failure criteria. Therefore, bilinear CZMs are used to simulate delamination and adhesive failure in Model I. The relationship between the stress and displacement of the upper and lower surfaces defines the constitutive model of CZMs (Fig. 4), and is described as a bilinear Traction-Separation Law (Fig. 5) [31]. The nominal traction stress consists of three components in 3D problems: t_n, t_s and t_t, which represent the normal (t_n) and the two shear tractions (t_s and t_t) respectively. The corresponding separations are denoted by δ_n, δ_s and δ_t. The nominal strains can be defined as

$$\varepsilon_n = \delta_n/T_0, \quad \varepsilon_s = \delta_s/T_0, \quad \varepsilon_t = \delta_t/T_0 \tag{8}$$

where T_0 is the initial thickness of the element. The initial linear elastic behavior is

$$\mathbf{t} = \begin{Bmatrix} t_n \\ t_s \\ t_t \end{Bmatrix} = \begin{bmatrix} K_{nn} & & \\ & K_{ss} & \\ & & K_{tt} \end{bmatrix} \begin{Bmatrix} \varepsilon_n \\ \varepsilon_s \\ \varepsilon_t \end{Bmatrix} \tag{9}$$

where K_{nn}, K_{ss} and K_{tt} represent the ratio between different stiffness coefficients and the nominal thickness respectively. The initial damage is evaluated by the following quadratic nominal stress criterion [32] expressed as

$$\left(\frac{\langle t_n \rangle}{t_n^0}\right)^2 + \left(\frac{t_s}{t_s^0}\right)^2 + \left(\frac{t_t}{t_t^0}\right)^2 = 1 \tag{10}$$

where $\langle\ \rangle$ is the Macaulay bracket, emphasizing that a purely compressive stress state does not initiate damage. Once the criterion is met, the material stiffness initiates a degradation process, as expressed by the following constitutive model:

$$\mathbf{t} = \begin{Bmatrix} t_n \\ t_s \\ t_t \end{Bmatrix} = (1-D)\begin{bmatrix} K_{nn} & & \\ & K_{ss} & \\ & & K_{tt} \end{bmatrix} \begin{Bmatrix} \varepsilon_n \\ \varepsilon_s \\ \varepsilon_t \end{Bmatrix} \tag{11}$$

where D ($0 \le D \le 1$) is the damage variable, evolving from initial damage (equals 0) to ultimate failure (approaches 1). The ultimate failure displacement of cohesive elements is defined by the fracture energy G^c, which is corresponding to the area under the traction-separation curve as shown in Fig. 5. The critical fracture energy can be calculated by the Benzeggagh-Kenane fracture criterion [33] expressed as

$$G^C = G_n^C + (G_s^C - G_n^C)\left(\frac{G_s^C + G_t^C}{G_n^C + G_s^C + G_t^C}\right)^\eta \tag{12}$$

where η is a material parameter, and is taken as 1.45 in this paper [34].

In Model II, Hashin-type failure criteria [35] are chosen to predict

Table 5
Detailed failure criteria of models.

Model	Failure criteria		
	Adherend	Adhesive	Interface of the adherend
I	Improved 3D Hashin/ Exponential progressive damage evolution	CZMs	CZMs (zero-thickness)
II	3D Hashin-type/ Improved anticlimactic damage evolution	CZMs	
III	3D Hashin-type/ Improved anticlimactic damage evolution	Distortion energy theory	

the damage of laminates, because the criteria include prediction of delamination. A sententious model is then established without interfacial cohesive elements. The expressions are shown in Table 7, and the initial damage criteria include six different failure types. In order to improve efficiency, an improved anticlimactic damage evolution law is developed based on the research by Camanho et al. [36] and Tserpes et al. [37]. In this damage evolution law, elastic constants are updated by multiplying constant degradation coefficients, which are listed in Table 7. The elastic constants of matrix tension and compression share the same degradation coefficients, so these two types of matrix damage can be unified. In the same way, fiber damage and delamination can be also unified. Thus, four field variables FV1, FV2, FV3, and FV4 can represent all types of damage (fiber-matrix shear-out, matrix tension or compression damage, delamination in tension or compression, and fiber tension or compression damage). A user subroutine VUSDFLD [30] is used to control material degradation by changing the field variables from 0 to 1. For the adhesive, the CZMs are still used in Model II, the same as in Model I.

In Model III, the distortion energy theory is adopted to predict the adhesive failure instead of the CZMs. According to this fundamental theory, the Von Mises yield criterion is used and the initiation of yielding is defined as

$$\sigma_s = \frac{1}{\sqrt{2}}\sqrt{(\sigma_1-\sigma_2)^2 + (\sigma_2-\sigma_3)^2 + (\sigma_3-\sigma_1)^2} \leqslant [\sigma] \tag{13}$$

where σ_1, σ_2 and σ_3 are the principal stress components, and σ_s is the yield stress. The Von Mises yield criterion can be programmed easily in VUSDFLD. Meanwhile, the 3D Hashin-type failure criteria are still chosen to predict the damage of laminates. Thus, in Model III, just one user subroutine VUSDFLD is used, in which the failure criteria of the adherend and the adhesive are programmed together.

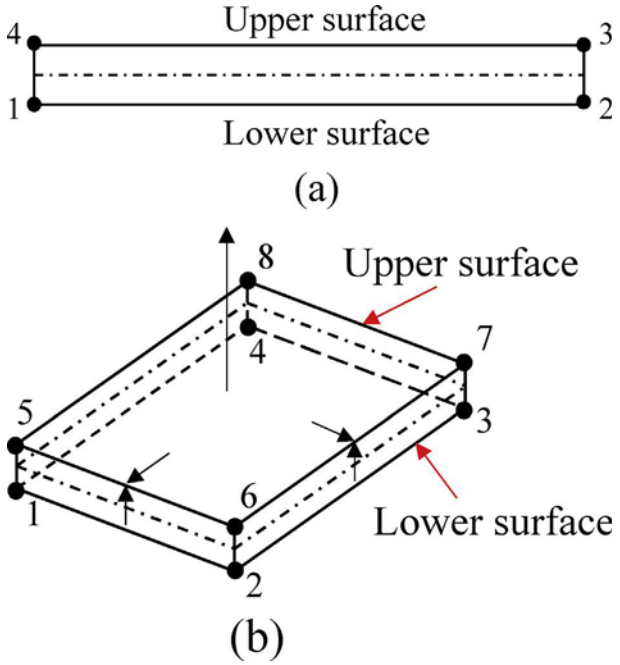

Fig. 4. Diagram of cohesive elements: (a) 2D elements; (b) 3D elements.

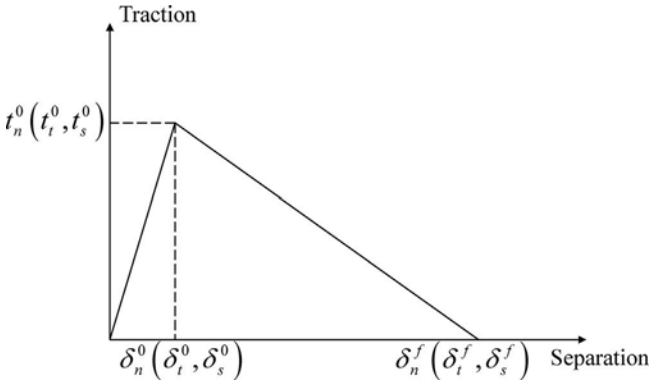

Fig. 5. Bilinear Traction-Separation Law.

3.2. Finite element models

3.2.1. Parametric modeling

A parameterized model of single-lap joints is established through a one-click program. The program is developed using the Python language, and a human–machine interaction window is developed based on ABAQUS RSG dialog builder tools [38]. The model parameters, such as model sizes and analysis settings, can be conveniently controlled by inputting parameters in the dialog box. Users can even

Table 6
Improved 3D Hashin failure criteria.

Failure type	Initial damage criterion
Fiber tension failure ($\varepsilon_1 > 0$)	$F_{ft}^2 = \left(\frac{\varepsilon_1}{\varepsilon_{1t}^f}\right)^2 + \left(\frac{\gamma_{12}}{\gamma_{12}^f}\right)^2 + \left(\frac{\gamma_{13}}{\gamma_{13}^f}\right)^2$
Fiber compression failure ($\varepsilon_1 < 0$)	$F_{fc} = -\frac{\varepsilon_1}{\varepsilon_{1c}^f}$
Matrix tension cracking ($\varepsilon_2 + \varepsilon_3 > 0$)	$F_{mt}^2 = \left[1-\left(\frac{\varepsilon_{2t}^f}{2\gamma_{23}^f}\right)^2\right]\frac{(\varepsilon_2+\varepsilon_3)}{\varepsilon_{2t}^f} + \left(\frac{\varepsilon_2+\varepsilon_3}{2\gamma_{23}^f}\right)^2 - \frac{\varepsilon_2\varepsilon_3}{(\gamma_{23}^f)^2} + \left(\frac{\gamma_{12}}{\gamma_{12}^f}\right)^2 + \left(\frac{\gamma_{13}}{\gamma_{13}^f}\right)^2 + \left(\frac{\gamma_{23}}{\gamma_{23}^f}\right)^2$
Matrix compression cracking ($\varepsilon_2 + \varepsilon_3 < 0$)	$F_{mc}^2 = \left[\left(\frac{\varepsilon_{2c}^f}{2\gamma_{23}^f}\right)^2 - 1\right]\frac{(\varepsilon_2+\varepsilon_3)}{\varepsilon_{2c}^f} + \left(\frac{\varepsilon_2+\varepsilon_3}{2\gamma_{23}^f}\right)^2 - \frac{\varepsilon_2\varepsilon_3}{(\gamma_{23}^f)^2} + \left(\frac{\gamma_{12}}{\gamma_{12}^f}\right)^2 + (\frac{\gamma_{13}}{\gamma_{13}^f})^2 + \left(\frac{\gamma_{23}}{\gamma_{23}^f}\right)^2$

Table 7
3D Hashin-type failure criteria and the improved anticlimactic damage evolution law.

Failure mode	Initial damage criterion	Improved anticlimactic damage evolution law
Fiber tension failure ($\sigma_1 > 0$)	$\left(\frac{\sigma_1}{Y_t}\right)^2 + \left(\frac{\tau_{12}}{S_{12}}\right)^2 + \left(\frac{\tau_{13}}{S_{13}}\right)^2 = 1$	$E_1' = 0.07E_1$
Fiber compression failure ($\sigma_1 < 0$)	$\left(\frac{\sigma_1}{X_c}\right)^2 = 1$	
Matrix tension cracking ($\sigma_2 > 0$)	$\left(\frac{\sigma_2}{Y_t}\right)^2 + \left(\frac{\tau_{12}}{S_{12}}\right)^2 + \left(\frac{\tau_{23}}{S_{23}}\right)^2 = 1$	
Matrix compression cracking ($\sigma_2 < 0$)	$\left(\frac{\sigma_2}{Y_c}\right)^2 + \left(\frac{\tau_{12}}{S_{12}}\right)^2 + (\frac{\tau_{23}}{S_{23}})^2 = 1$	$E_2' = 0.2E_2$, $G_{12}' = 0.2G_{12}$, $G_{23}' = 0.2G_{23}$
Fiber–matrix shear-out	$\left(\frac{\sigma_1}{X_c}\right)^2 + \left(\frac{\tau_{12}}{S_{12}}\right)^2 + \left(\frac{\tau_{13}}{S_{13}}\right)^2 = 1$	$G_{12}' = 0$, $\nu_{12}' = 0$
Delamination in tension ($\sigma_3 > 0$)	$\left(\frac{\sigma_3}{Z_t}\right)^2 + \left(\frac{\tau_{23}}{S_{23}}\right)^2 + \left(\frac{\tau_{13}}{S_{13}}\right)^2 = 1$	$E_3' = 0$, $G_{13}' = 0$, $G_{23}' = 0$, $\nu_{13}' = 0$, $\nu_{23}' = 0$
Delamination in compression ($\sigma_3 < 0$)	$\left(\frac{\sigma_3}{Z_c}\right)^2 + \left(\frac{\tau_{23}}{S_{23}}\right)^2 + \left(\frac{\tau_{13}}{S_{13}}\right)^2 = 1$	

X_t, X_c, Y_t, Y_c, Z_t, Z_c, $S_{ij}(i, j = 1, 2, 3)$ the corresponding failure strengths.
E_1, E_2, E_3, G_{12}, G_{13}, G_{23}, ν_{12}, ν_{13}, ν_{23} the initial elastic properties.
E_1', E_2', E_3', G_{12}', G_{13}', G_{23}', ν_{12}', ν_{13}', ν_{23}' the weakened elastic properties.

make a decision whether to add interface elements or not. As a result, the research process is simplified.

3.2.2. Model details

Based on the abovementioned failure criteria and parametric modeling program, detailed explicit analysis models are established (Fig. 6). For these models are of the same size, most model settings are the same, and the only difference is in mesh types. The mesh type of each model is shown in Table 8 and Fig. 7. The adherend is modeled by eight-node 3D linear brick elements with reduced integration (C3D8R) in all models, and the enhanced stiffness relaxation method is used to prevent hourglassing of the reduced integration elements. Eight-node 3D cohesive elements (COH3D8) are adopted to model the adhesive of Model I and Model II while C3D8R are applied to the adhesive of Model III. Meanwhile, COH3D8 are applied to the interface of the adherend in Model I (Fig. 7(a)), and the interface elements are defined as zero-thickness to

Table 8
Typical elements of different models.

Model	Element		
	Adherend	Adhesive	Interface of the adherend
I	C3D8R	COH3D8	COH3D8
II	C3D8R	COH3D8	
III	C3D8R	C3D8R	

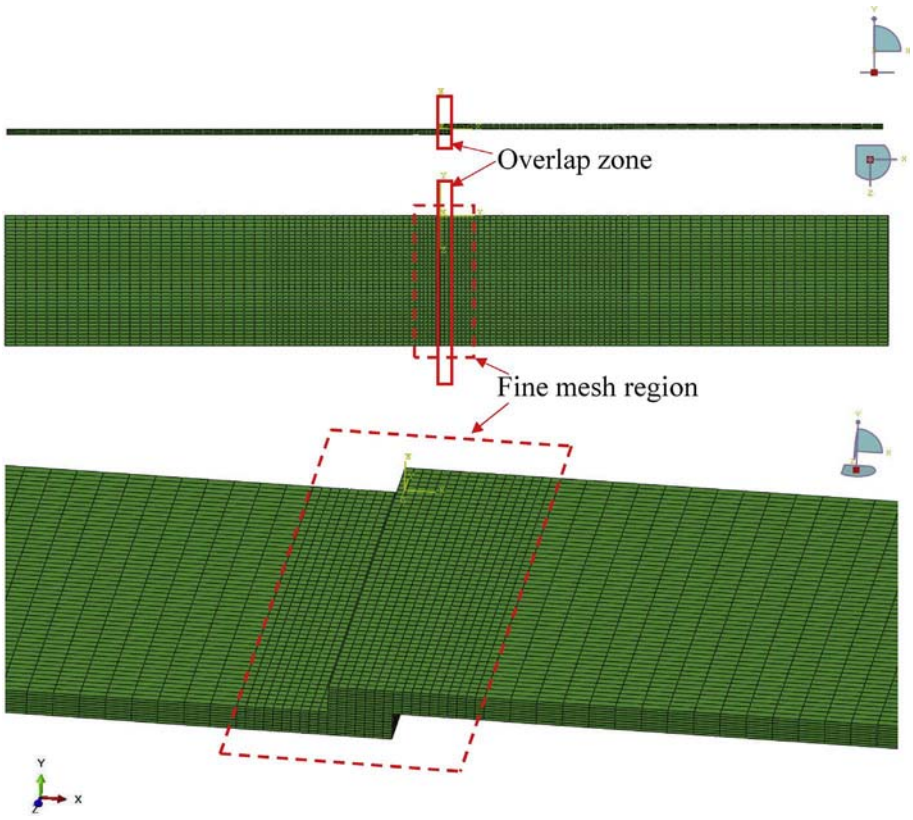

Fig. 6. Explicit analysis models with fine mesh regions.

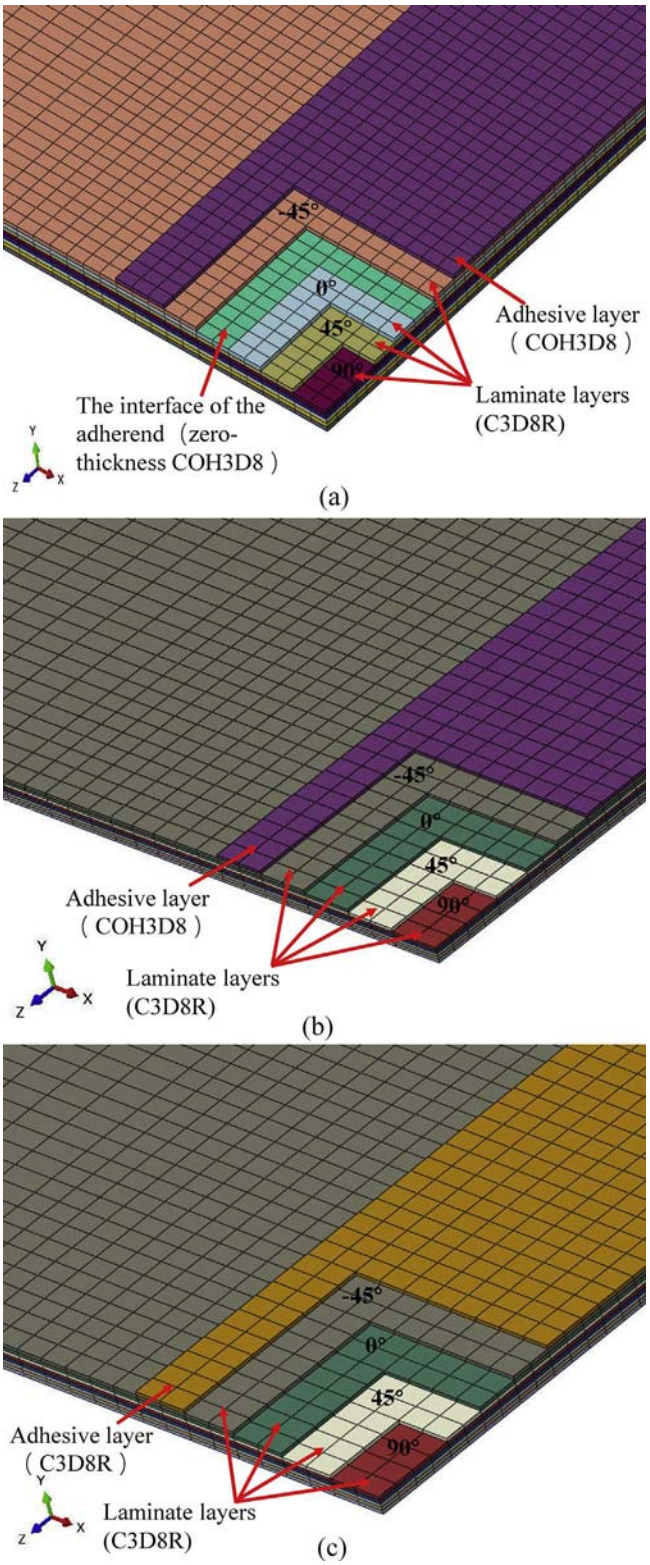

Fig. 7. Mesh types of different models: (a) Model I; (b) Model II; (c) Model III.

simulate delamination. The computing time increases dramatically when cohesive elements are used [39]. Since delamination occurs between the first two layers adjacent to the adhesive in experiments, interfacial cohesive elements are only placed between the first two layers to decrease modeling complexity and computation costs. The overlap area, including the localized region around it, is discretized with the fine mesh to improve computation accuracy (Fig. 6). All models are fixed at one end and subjected to a uniform tensile displacement at the other end.

3.2.3. Element deletion

Although explicit methods can overcome the convergence problems resulting from divergent results of iterative computations and ill-conditioned solutions for simultaneous equations, the methods may still have other convergence problems caused by element distortion. Element deletion is a practical numerical strategy to overcome this problem. Thus, an element deletion technique proposed by Hu et al. [22] is adopted and improved to avoid element distortion of laminates, considering material failure and large volume changes of elements. Material failure is determined by damage variables or field variables, which are calculated by the failure criteria mentioned in the above sections, and the maximum damage variables representing material failure are taken as 0.999. Critical volume changes of 3D elements is defined by a deformation-based maximum strain criterion as follows [40]:

$$|\varepsilon_i| = \varepsilon_{max} \quad (i = 1, 2, 3) \tag{14}$$

where $\varepsilon_i (i = 1, 2, 3)$ are the normal strain components and ε_{max} is the maximum strain. The value of ε_{max} is discussed later in the next section. At an integration point, once the damage variable has approached 1 or the strain component has satisfied Eq. (14), the contribution of this point to the element stiffness matrix is ignored. For the complete deletion of elements, two combined deletion criteria can be further considered [22]: strong or weak combined deletion criterion. If an element needs to be deleted, the strong combined deletion criterion requires that all the integration points in the element either fail or satisfy Eq. (14), whereas the weak one only requires one integration point. The strong combined deletion criterion is recommended for most cases and the weak one is more suitable for extremely severe element distortion and material crushing [22]. Considering that the loading process is slow, and the local distortion is not severe, strong combined deletion criterion is employed in this paper.

The deletion criterion can be implemented in user subroutines using the deletion state variable of the integration point, and the state variable number is specified to control the element deletion flag. Generally, the deletion state variable can be set to 1 or 0, meaning that the integration point is active, or that the integration point is ignored, respectively. Once a point has been flagged as ignored, it cannot be reactivated. Besides, the deletion of cohesive elements can be directly defined in ABAQUS with the damage index being 0.99.

4. Results and discussion

4.1. Maximum strain of element deletion

Different values of ε_{max} are investigated to find a suitable one for element deletion. Taking Model I as an example, the simulation results of Group C are provided in Fig. 8, with ε_{max} equal to 2%, 7%, 12%, 15%, 18%, 20% and 22%. It can be seen that the maximum failure load is significantly low when ε_{max} equals 2%, 7%, 12% and 15%, resulting from premature deletion of elements. The premature deletion of elements can be observed at the edge of the overlap area in both sides of the joint when ε_{max} equals 2% (Fig. 8(a)), but in only one side of the joint when ε_{max} equals 12% (Fig. 8(b)) because of the increase of ε_{max}. However, when ε_{max} equals 18%, 20% and 22%, hardly are any elements prematurely deleted (Fig. 8(c)), and the simulation results are closely consistent, indicating that the value of ε_{max} for converged results can be taken as 20%. Similar results can be obtained in other models, and this value is approximately consistent with the one used in other studies [22,41].

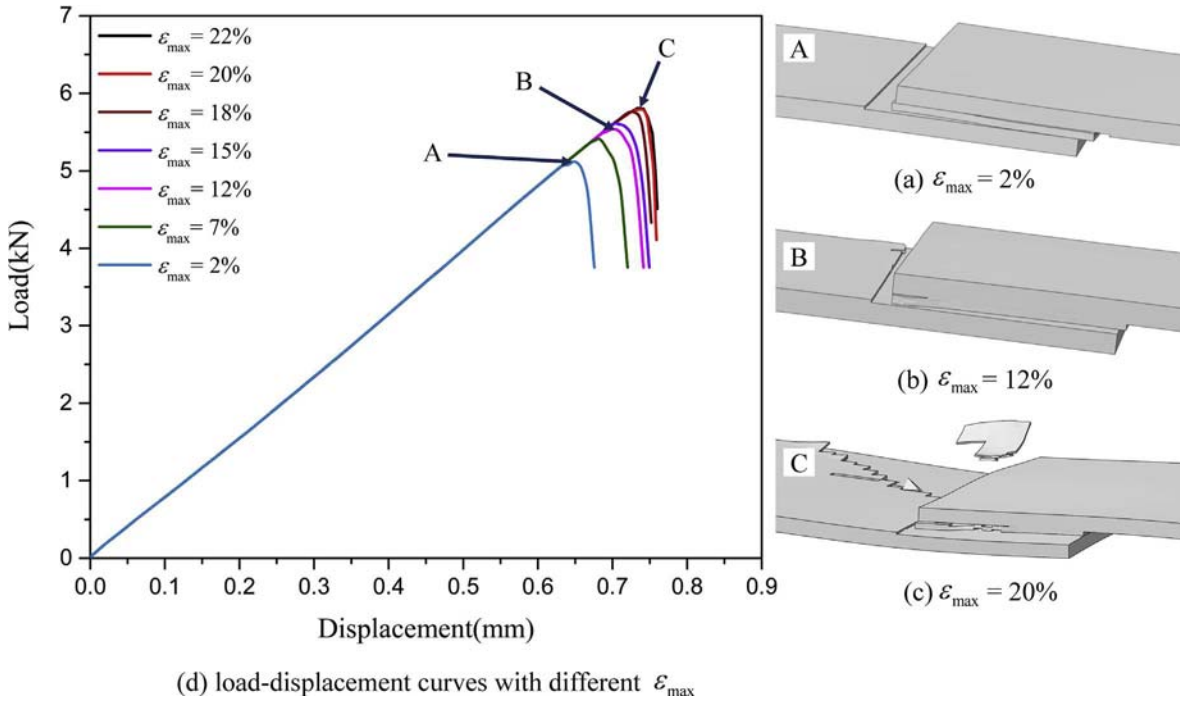

Fig. 8. Simulation results of Group C in Model I using different values of ε_{max} . The graphs "A, B, C" represent the element deletion in three typical conditions.

Table 9
Comparisons of the maximum failure load of numerical and average experimental results.

Group	Maximum failure load (kN)			
	Average experimental results	Numerical results (Relative error)		
		Model I	Model II	Model III
A	1.85	1.77 (4.3%)	1.88 (1.6%)	1.87 (1.0%)
B	3.61	3.52 (2.4%)	3.71 (2.8%)	3.73 (3.3%)
C	6.08	5.80 (4.7%)	5.97 (1.8%)	6.22 (2.3%)

4.2. Load-displacement curves

Table 9 and Fig. 9 show the comparison of numerical and experimental results. All numerical curves are consistent with experiments with different overlap lengths, and the maximum relative error of the failure load between numerical and average experimental results is less than 10%. The relative error is reasonable and may be caused by the following reasons: (i) The specimens contain initial cracks and manufacture errors; (ii) The clamping ends contain tiny slippages. Besides, the maximum failure load of Model I is slightly lower than the test results, while those of Model II and Model III tend to be slightly higher, indicating that Model I is relatively conservative. The curves are basically in the linear ascending segment during the prophase and begin to decline gradually after reaching the maximum load. Due to the explicit algorithms, the numerical curves have some fluctuations, but can reach the maximum load with no convergence problems. Besides, Model I is nearly twice computationally expensive than the others.

4.3. Failure modes of numerical simulations

Since all the damage occurs near the overlap area, the localized regions around the overlap area are taken as viewing zones. In order to compare numerical and experimental results conveniently, the failure contours of simulations are arranged in accordance with Fig. 10. The upper and lower plates are placed relative to each other, and the surfaces adjoining the adhesive are upward.

Fig. 11 shows that all models share similar simulation results when the overlap length is 2.5 mm. Because the bearing capacity of the narrow adhesive layer is weak, the failure mode of these models is the complete adhesive failure (Fig. 11(a)) with no obvious damage of the adherend (Fig. 11(b) to (e)), consistent with Mode A.

Fig. 12 shows that the adhesive layer is partly damaged in all models when the overlap length is 5.0 mm, and the damage range of Model II is slightly larger (Fig. 12(a)). Nevertheless, only Model I and Model III have similar delamination in the undamaged area of the adhesive and along the fiber direction of the non-lap zone (Fig. 12(d)), consistent with Mode B. In Model I, zero-thickness cohesive elements are damaged, indicating the separation between the first two layers; in Model III, the field variable of the delamination (FV3) reaches failure criteria almost in the same area. Matrix damage and slight fiber damage can be also found in the delamination area of Model I and Model III (Fig. 12(c) and Fig. 12(e)), coinciding with the fiber pull-out in experiments. Except at some stress concentration positions, no delamination, matrix damage and fiber damage can be observed in Model II, which is inconsistent with Mode B (Fig. 12(c) to (e)).

Fig. 13 shows that the adhesive is intact in all models, when the overlap length is 10.0 mm. In Model I and Model III, delamination (Fig. 13(d)) occurs in the overlap area of the lower plates, and extends outwards along the fiber direction. The matrix damage and fiber damage of Model I and Model III (Fig. 13(c) and (e)) are basically consistent with the fiber pull-out and fiber fracture in Region C-3 and Region C-4 of Fig. 3, respectively. Moreover, the upper plates of Model I and Model III also have delamination around a corner, which is consistent with Mode C. However, in Model II, delamination is restricted to the overlap area, and the matrix damage and fiber damage are

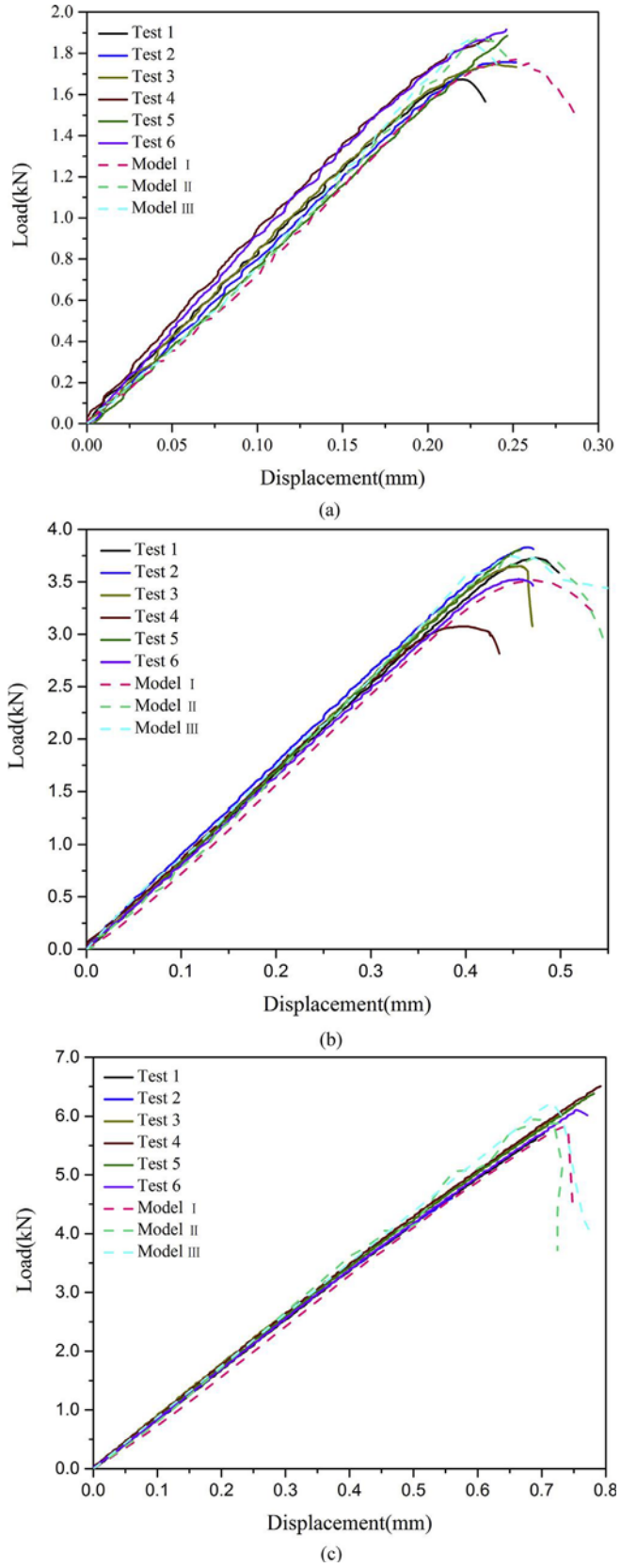

Fig. 9. Comparisons of the load-displacement curves between numerical simulations and experiments: (a) Group A; (b) Group B; (c) Group C.

concentrated at the stress concentration positions (Fig. 13(c) to (e)).

Overall, all models can predict the experimental Mode A, and only Model I and Model III can predict the experimental Mode B and Mode C. Model II cannot simulate the experimental results involving delamination. Besides, Model I is more accurate than Model III in terms of prediction of matrix damage and fiber damage, because of the progressive damage evolution law. It is noticed that the influence of fiber-matrix shear-out failure is unapparent, and delamination always occurs along with fiber pull-out.

4.4. Effect of cohesive elements on delamination

In order to study the effect of zero-thickness cohesive elements on delamination, the models with the 5.0 mm overlap length are selected. The path along the through-thickness direction of the lower plate and near the delamination position (Fig. 14) is picked. The interlaminar stresses on the path are output. Because the interlaminar shear stress τ_{23} is relatively small, only the interlaminar normal stress σ_{33} and the interlaminar shear stress τ_{13} are analyzed. Fig. 15 shows the distributions of σ_{33} and τ_{13} near the ultimate failure point of all models. The y-axis represents stress, and the x-axis represents the sequence ID of the nodes along the path. The stress distribution of all models is basically consistent from the third layer to the eighth layer. But significant differences can be observed around the first and second layer, and delamination exactly occurs here. Different from Model II, interlaminar stresses are changed dramatically between the first and second layer in Model I, because zero-thickness interfacial cohesive elements are located here. This change positively affects the prediction of delamination and leads to failure of interface elements, even if the overall interlaminar stress level is not high. Although Model III has no interface elements either, the change of adhesive element type results in improvement of the stress level in the first two layers, and delamination consequently occurs.

When the overlap length is 10.0 mm, the interlaminar stresses are high enough, and delamination of laminates can be observed in all models. But delamination of Model II is only restricted to the overlap area. Fig. 16 shows the stress contours and the corresponding strain contours of the first layer under the condition of ultimate failure in Model II. Due to the evolution law of anticlimactic damage used in Model II, the elastic parameters (E_3, G_{13}, G_{23}, ν_{13} and ν_{23}) of laminates are suddenly reduced in the delamination area. According to Eq. (15), the capacity of bearing interlaminar tension, compression and shear has catastrophic deterioration. The stresses (S_{33}, S_{13} and S_{23}) associated with interlaminar damage dramatically decrease (close to 0), while the corresponding strains (LE_{33}, LE_{13} and LE_{23}) dramatically increase (close to 0.2) (Fig. 16), indicating the loss of interlaminar bearing capacity and the dramatically increased relative displacement of the upper and lower surfaces of the first layer. Meanwhile, the adhesive in Model II adopts the CZMs, which contains only three components (S_{33}, S_{13} and S_{23}) in 3D problems. Therefore, when the capacity of bearing interlaminar stresses (S_{33}, S_{13} and S_{23}) catastrophically deteriorates in most overlap areas of the first layer, stresses of the upper plate cannot be transferred to the lower plate through the shearing action between the cohesive adhesive layer and the plates. As a result, Model II loses the carrying capacity and gets the mispredicted damage propagation.

$$\begin{Bmatrix} \varepsilon_{11} \\ \varepsilon_{22} \\ \varepsilon_{33} \\ \gamma_{12} \\ \gamma_{13} \\ \gamma_{23} \end{Bmatrix} = \begin{bmatrix} 1/E_1 & -\nu_{21}/E_2 & -\nu_{31}/E_3 & & & \\ -\nu_{12}/E_1 & 1/E_2 & -\nu_{32}/E_3 & & & \\ -\nu_{13}/E_1 & -\nu_{23}/E_2 & 1/E_3 & & & \\ & & & 1/G_{12} & & \\ & & & & 1/G_{13} & \\ & & & & & 1/G_{23} \end{bmatrix} \begin{Bmatrix} \sigma_{11} \\ \sigma_{22} \\ \sigma_{33} \\ \sigma_{12} \\ \sigma_{13} \\ \sigma_{23} \end{Bmatrix} \tag{15}$$

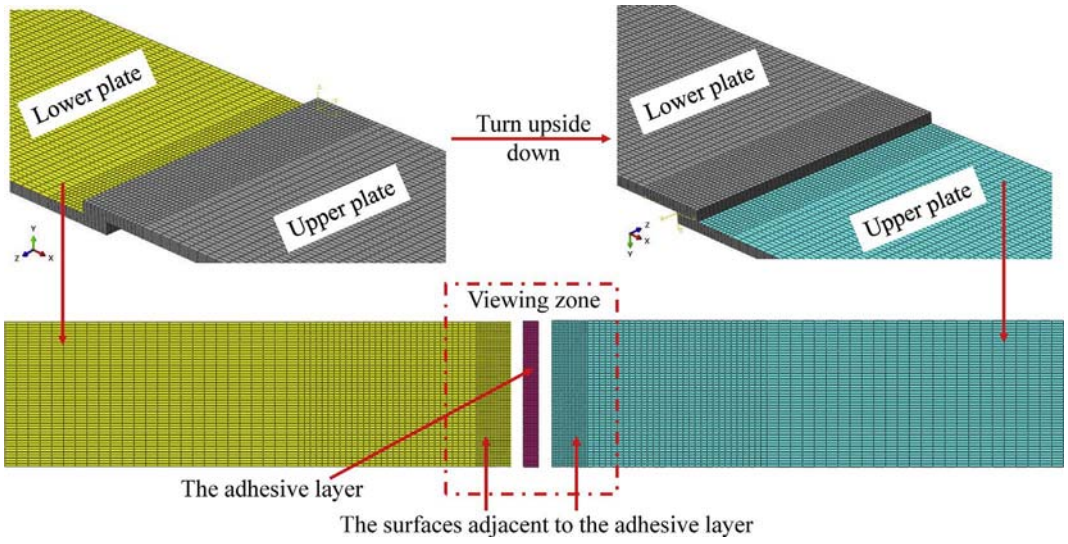

Fig. 10. Viewpoint of failure contours.

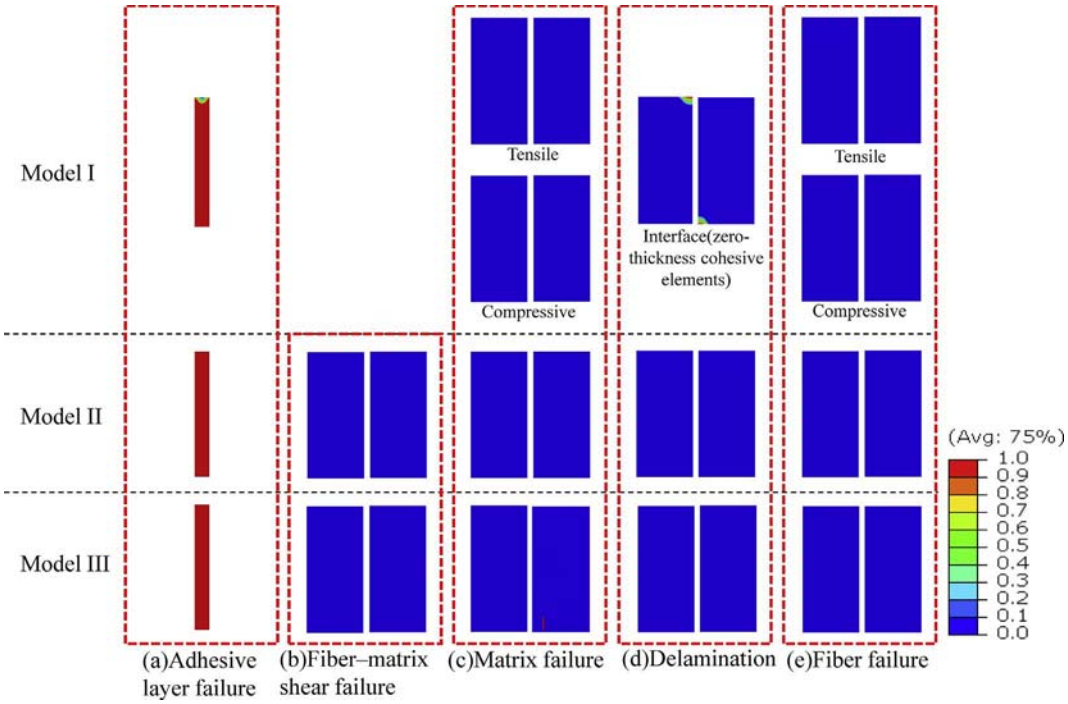

Fig. 11. Failure contours of Model I, II and III (L = 2.5 mm).

4.5. Stress distribution of the adhesive

To study the stress distribution of the adhesive, Model I with the 10.0 mm overlap length is chosen in this paper because of its complicated failure mode and accurate numerical results. A path in the middle of the adhesive layer along the tensile direction is picked and the stress on the path is output. Based on the load–displacement curve, four representative loading points are selected to reflect the stress evolution process of the adhesive. The loading points from 1 to 4 represent the process from the initial loading to the ultimate failure. Since the shear stress τ_{23} is relatively small, only the normal stress σ_{33} and the shear stress τ_{13} are analyzed. As a comparison, an implicit result is given by the method used in Ref. [18]. Fig. 17 describes σ_{33} and τ_{13} of the adhesive of explicit and implicit methods, respectively. It can be found that the stress curves of Model I share same distribution with the corresponding curves given by the implicit method.

Fig. 17(a) and (b) show the curves of the normal stress σ_{33}. They are symmetrically “W-shaped”. The value of the normal stress is low and

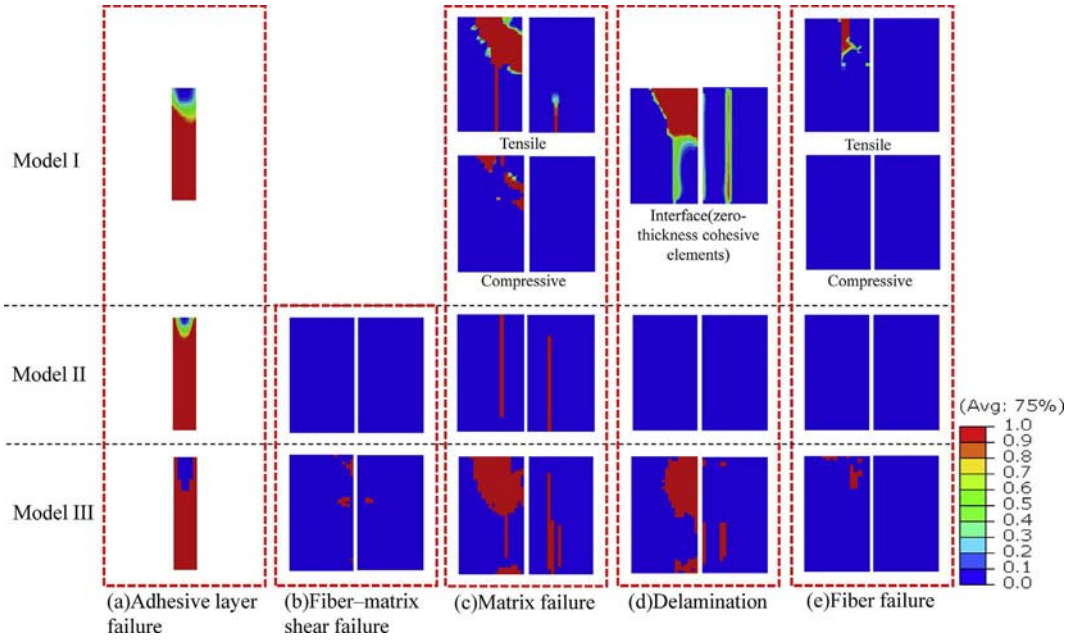

Fig. 12. Failure contours of Model I, II and III (L = 5.0 mm).

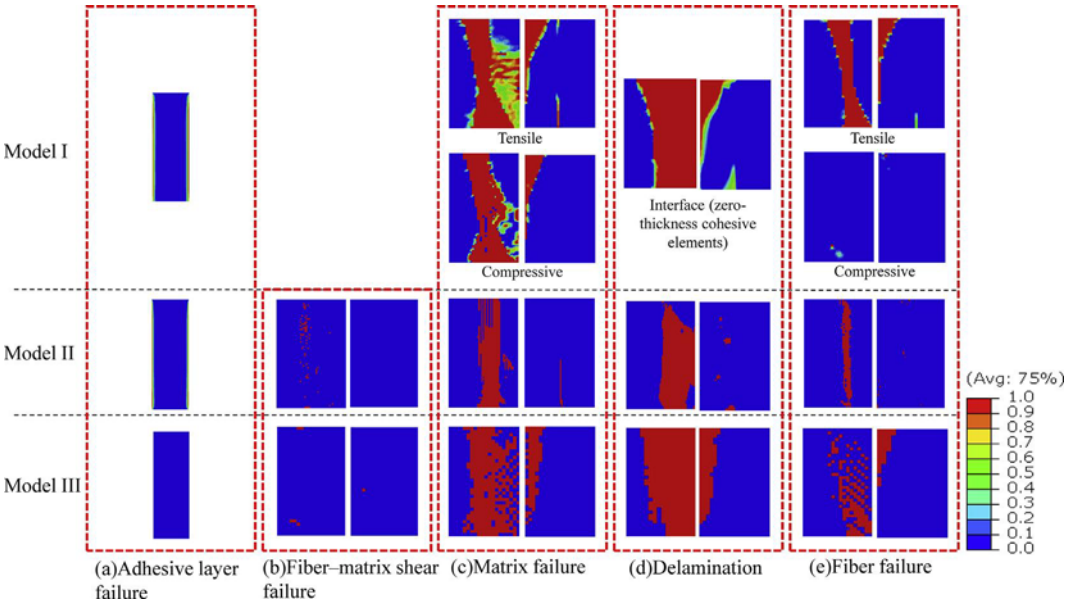

Fig. 13. Failure contours of Model I, II and III (L = 10.0 mm).

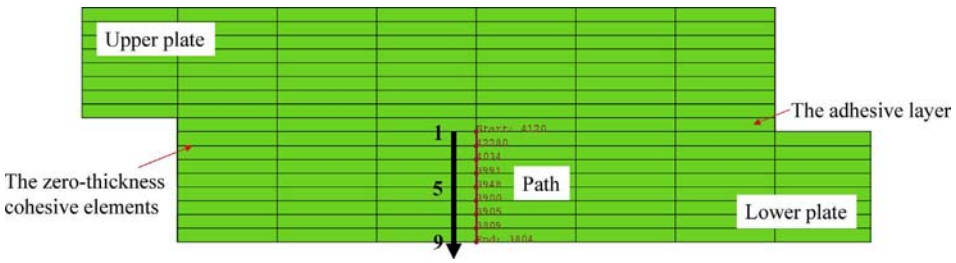

Fig. 14. Path along the through-thickness direction of the lower plate.

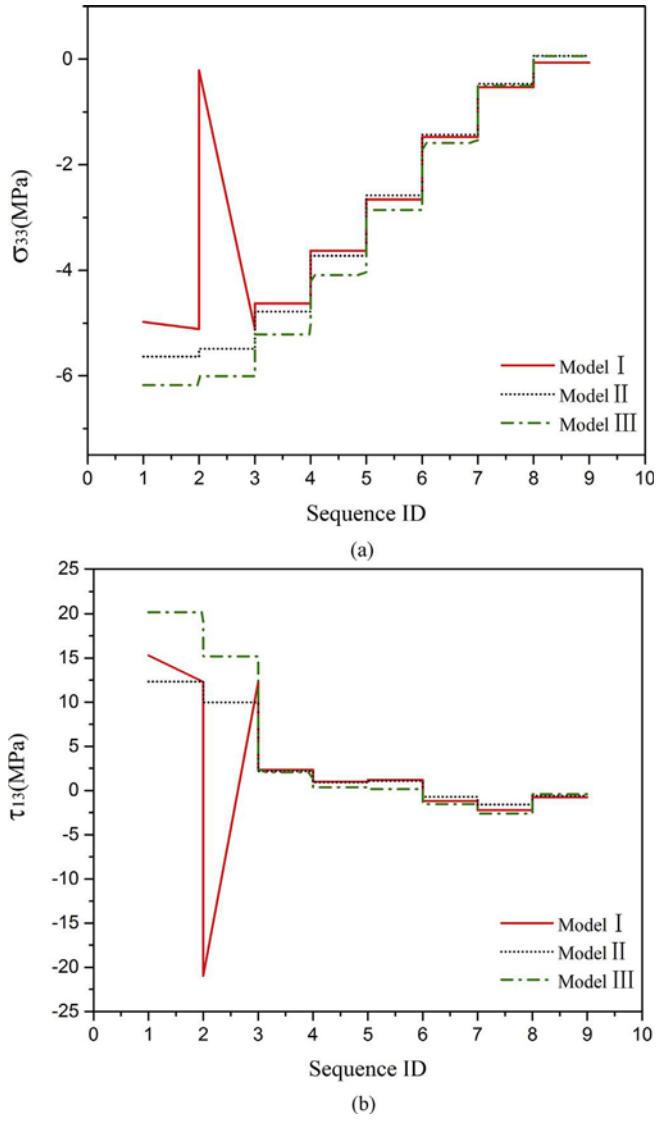

Fig. 15. Distribution of interlaminar stresses along the through-thickness direction of the lower plate: (a) normal stress σ_{33}; (b) shear stress τ_{13}.

negative in the middle area of the adhesive layer, but increases rapidly near both ends of the overlap area and turns to be positive. Furthermore, the closer to the ends, the faster σ_{33} grows. The reason is that additional bending moments exist at both ends of the overlap area with an effect of peeling off, and the effect decreases when the positions are away from the ends. As the loading displacement increases, the additional bending moments enhance. Thus, the positive stress and the absolute value of the negative stress increase in the loading process. The groove of the normal stress curves becomes narrower. Fig. 17(c) and (d) describe the shear stress τ_{13} , which is significantly greater than σ_{33}. However, it cannot be concluded that τ_{13} is the dominant stress of the adhesive failure, because the collapsing strength of each damage form is different. Due to the additional bending moments, the stress value of τ_{13} is also higher at both ends of the overlap area. As the loading displacement increases, the peak stress moves toward the middle region and the distribution of shear stress changes from “U-shaped” curves to “M-shaped” curves.

5. Conclusions

Three parameterized 3D explicit finite element models are developed to investigate different tensile failure modes of adhesive-bonded composite single-lap joints of different overlap lengths. User subroutines based on various failure criteria and element deletion techniques are widely used. Compared with the experimental results, the accuracy, efficiency and applicability of these models are comprehensively discussed in terms of load-displacement curves and failure morphology. The effect of cohesive elements on delamination and the stress distribution of the adhesive are analyzed in the end. The following conclusions are drawn:

(1) The tensile failure behavior is closely related to overlap lengths. As the overlap length increases, the failure load and the longitudinal failure displacement rise, and failure modes gradually change from adhesive failure to delamination of laminates. Delamination always occurs with the fiber pull-out.
(2) High efficiency and acceptable accuracy of 3D explicit models are demonstrated. All numerical load-displacement curves can reflect the actual situation of the test curves without convergence problems. Prediction of failure morphology depends on model types. All models can be considered only when adhesive failure occurs. Once delamination occurs in laminates, Model I and Model III perform better. Model I is more accurate in terms of prediction of matrix damage and fiber damage, but is more computationally expensive than the other two models. Thus, Model III is a prior option when high precision is not required. In the case of requirement for high accuracy, Model I should be adopted.
(3) Using cohesive interface elements significantly affects the distribution of interlaminar stress of laminates and plays a positive role in prediction of delamination. But when 3D solid elements and anticlimactic damage evolution laws are applied in laminates, using cohesive elements to predict damage propagation of adhesive layer can result in mistakes.
(4) The stress curves of the adhesive in Model I are consistent with the corresponding curves given by the implicit method. The maximum normal stress (σ_{33}) and shear stress (τ_{13}) both occur on the overlap ends, while the minimum stresses occur in the middle region. The stresses of the adhesive increase in the loading process and the effect of peeling off gradually extends toward the middle region of overlap areas.

Acknowledgements

This research did not receive any specific Grant from funding agencies in the public, commercial, or not-for-profit sectors.

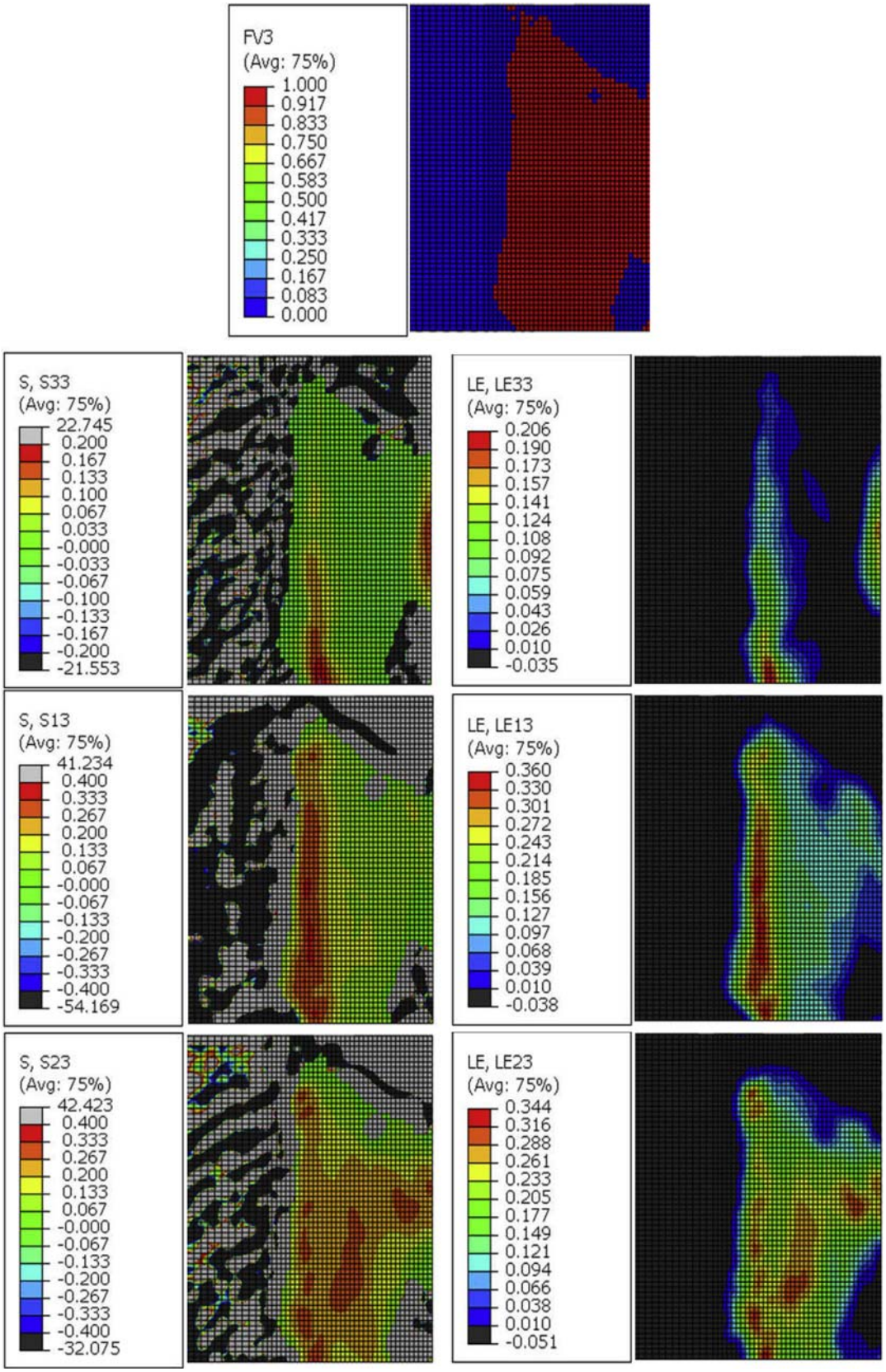

Fig. 16. Stress contours and corresponding strain contours of the delamination area in Model II.

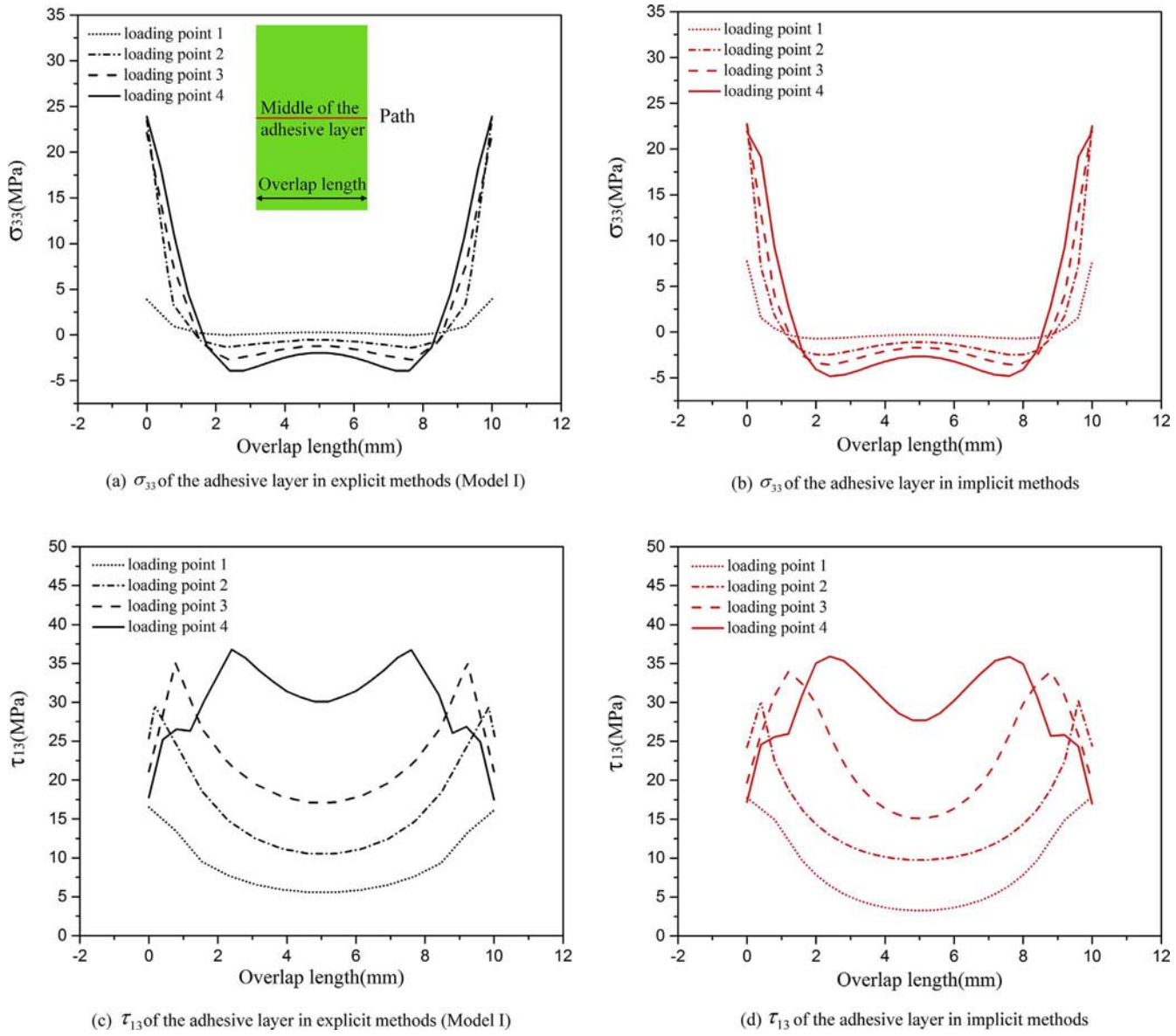

Fig. 17. Normal and shear stress distribution of the adhesive along the tensile direction: (a) σ_{33} in Model I; (b) σ_{33} in implicit methods; (c) τ_{13} in Model I; (d) τ_{13} in implicit methods.

Appendix A. Supplementary data

Supplementary data associated with this article can be found, in the online version, at http://dx.doi.org/10.1016/j.compstruct.2018.05.134.

References

[1] Goland M, Reissner E. The stresses in cemented joints. J Appl Mech 1944;11(1):A17–27.
[2] Hart-Smith LJ. Adhesive-bonded single-lap joints. Hampton, MI: Langley Research Center; 1973.
[3] Adams RD, Peppiatt NA. Stress analysis of adhesive-bonded lap joints. J Strain Anal Eng Des 1974;9(3):185–96.
[4] Renton WJ, Vinson JR. The efficient design of adhesive bonded joints. J Adhes 1975;7(3):175–93.
[5] Renton WJ, Vinson JR. Analysis of adhesively bonded joints between panels of composite materials. J Appl Mech 1977;44(1):101–6.
[6] Allman DJ. A theory for elastic stresses in adhesive bonded lap joints. Q J Mech Appl Math 1977;30(4):415–36.
[7] Harris JA, Adams RA. Strength prediction of bonded single lap joints by non-linear finite element methods. Int J Adhes Adhes 1984;4(2):65–78.
[8] Pickett AK, Hollaway L. The analysis of elastic-plastic adhesive stress in bonded lap joints in FRP structures. Compos Struct 1985;4(2):135–60.
[9] Gunnion AJ, Herszberg I. Parametric study of scarf joints in composite structures. Compos Struct 2006;75:364–76.
[10] Andruet RH, Dillard DA, Holzer SM. Two- and three-dimensional geometrical nonlinear finite elements for analysis of adhesive joints. Int J Adhes Adhes 2001;21(1):17–34.
[11] Gonçalves J, Moura M, Castro P. A three-dimensional finite element model for stress analysis of adhesive joints. Int J Adhes Adhes 2002;22(5):357–65.
[12] Wahab MA, Ashcroft IA, Crocombe AD. Prediction of fatigue thresholds in adhesively bonded joints using damage mechanics and fracture mechanics. J Adhes Sci Technol 2001;15(7):763–81.
[13] Anyfantis KN, Tsouvalis NG. A 3D ductile constitutive mixed-mode model of cohesive elements for the finite element analysis of adhesive joints. J Adhes Sci Technol 2013;27(10):1146–78.
[14] Blackman BK, Hadavinia H, Kinloch AJ. The use of a cohesive zone model to study the fracture of fiber composites and adhesively-bonded joints. Int J Fract 2003;119(1):25–46.
[15] Li S, Thoules MD, Waas AM. Competing failure mechanisms in mixed-mode fracture of an adhesively bonded polymer-matrix composite. Int J Adhes Adhes 2006;26(8):609–16.
[16] Li S, Thoules MD, Waas AM. Mixed-mode cohesive-zone models for fracture of an adhesively bonded polymer-matrix composite. Eng Fract Mech 2006;73(1):64–78.
[17] Moura M, Gonçalves J. Cohesive and continuum mixed-mode damage models applied to the simulation of the mechanical behavior of bonded joints. Int J Adhes Adhes 2008;28(8):419–26.
[18] Li J, Yan Y, Liang Z. Experimental and numerical study of adhesively bonded CFRP

scarf-lap joints subjected to tensile loads. J Adhes 2016;92(1):1–17.
[19] Luo H, Yan Y, Zhang T. Progressive failure and experimental study of adhesively bonded composite single-lap joints subjected to axial tensile loads. J Adhes Sci Technol 2016;30(8):1–21.
[20] Liu P, Cheng X, Wang S. Numerical analysis of bearing failure in countersunk composite joints using 3D explicit simulation method. Compos Struct 2016;138:30–9.
[21] Neumayer J, Koerber H, Hinterhölzl R. An explicit cohesive element combining cohesive failure of the adhesive and delamination failure in composite bonded joints. Compos Struct 2016;146:75–83.
[22] Hu XF, Haris A, Ridha M, et al. Progressive failure of bolted single-lap joints of woven fibre-reinforced composites. Compos Struct 2018;189:443–54.
[23] Linde P, Pleitner J, Boer H, Carmone C. Modelling and simulation of fiber metal laminates. In: The 17th annual ABAQUS Users' Conference, Boston, 24–27 May 2004. p. 421–439.
[24] Hashin Z. Failure criteria for unidirectional fiber composites. J Appl Mech 1980;47:329–34.
[25] Yang L, Yan Y. Progressive damage analysis method and experimental investigation of composite end frame structure. J Beijing Univ Aeronaut Astronaut 2012;38:931–5.
[26] Huang CH, Lee YJ. Experiments and simulation of the static contact crush of composite laminated plates. Compos Struct 2003;61(3):265–70.
[27] Wang Y, Tong M, Zhu S. Three-dimensional continuum damage mechanics model of progressive failure analysis in fiber-reinforced composite laminates. In: 50th AIAA/ASME/ASCE/AHS/ASC structures, structural dynamics, and materials conference, California, 04–07 May 2009.
[28] Raimondo L, Iannucci L, Robinson P. A progressive failure model for mesh-size-independent FE analysis of composite laminates subject to low-velocity impact damage. Compos Sci Technol 2012;72:624–32.
[29] Tian Z, Yan Y, Ye J. An analytical constitutive model for progressive damage analysis of three-dimensional braided composites. Polym Compos 2017.
[30] HIbbitt, Karlsson & Sorensen, Inc. ABAQUS v5.8 Users' Manual 1998; Section 1.2.
[31] Liu P, Gu Z, Peng X. Finite element analysis of the influence of cohesive law parameters on the multiple delamination behaviors of composites under compression. Compos Struct 2015;131:975–86.
[32] Campilho R, Banea M, Neto J. Modelling adhesive joints with cohesive zone models: effect of the cohesive law shape of the adhesive layer. Int J Adhes Adhes 2013;44(7):48–56.
[33] Benzeggagh ML, Kenane M. Measurement of mixed-mode delamination fracture toughness of unidirectional glass/epoxy composites with mixed-mode bending apparatus. Compos Sci Technol 1996;56:439–49.
[34] Camanho PP, Dávila CG. Mixed-mode decohesion finite elements for the simulation of delamination in composite materials. NASA Technical Report 2002; NASA/TM-2002-211737.
[35] Papanikos P, Tserpes KI, Pantelakis S. Modelling of fatigue damage progression and life of CFRP laminates. Fatigue Fract Eng Mater Struct 2010;26(1):37–47.
[36] Camanho PP, Matthews FL. A progressive damage model for mechanically fastened joints in composite laminates. J Compos Mater 1999;33:2248–80.
[37] Tserpes KI, Labeas G, Papanikos P. Strength prediction of bolted joints in graphite/epoxy composite laminates. Compos B Eng 2002;33(7):521–9.
[38] HIbbitt, Karlsson & Sorensen, Inc. ABAQUS v5.8 Users' Manual 1998; Section 82.4.
[39] Zhang J, Zhang X. An efficient approach for predicting low-velocity impact force and damage in composite laminates. Compos Struct 2015;130:85–94.
[40] Dassault Systemes Simulia Corp., Providence, RI, USA, VUMAT for Fabric Reinforced Composites, SIMULIA Answer 3749. 2008. https://iam.3ds.com/ (accessed 02.03.16).
[41] Falzon BG, Wei T. Virtual testing of composite structures: progress and challenges in predicting damage, residual strength and crashworthiness. The structural integrity of carbon fiber composites. Springer International Publishing; 2017.